Proof-of-concept finite element analysis of a novel hybrid inter-module connection

D-A Corfar[1], K D Tsavdaridis[2]
[1] City, University of London, Northampton Square, London, EC1V 0EH, UK
[2] City, University of London, Northampton Square, London, EC1V 0EH, UK

E-mail: Konstantinos.Tsavdaridis@city.ac.uk

Abstract. Inter-module connections (IMCs) play a crucial role in the structural behaviour of steel Modular Building Systems (MBSs) by ensuring the vertical and horizontal load-transfer paths between modules, yet existing designs display limited disassembly opportunities and lack damage control features. This study introduces a novel, hybrid demountable IMC comprising bespoke corner fittings, a resilient high-damping rubber core and a shape-memory alloy (SMA) bolt. Proof-of-concept connection tests have been carried out using validated, continuum finite element analysis (FEA) to determine the mechanical behaviour of the proposed IMC with respect to the main deformation modes expected to occur in the joints of tall steel MBSs under the combined effect of vertical and horizontal loading. Main findings show that both the HDR core and the SMA bolt contribute effectively to the overall hybrid response of the IMC under tension and combined compression and shear loading, preventing the formation of significant plastic damage in the MBS's corner fittings to facilitate reusability of modules.

1. Introduction

Steel Modular Building Systems (MBSs) are a modern method of construction (MMC) that has gained a lot of traction due to well-established benefits such as halved construction times [1], lower capital costs [2], reduced on-site labour [3], less construction waste [4] and safer work sites [5]. Moreover, technological advancements achieved in Off-Site Manufacturing (OSM), Off-Site Construction (OSC) and Building Information Modelling (BIM) have accelerated the expansion of steel MBSs within the high-rise construction sector, where pre-finished corner-supported volumetric modules are typically assembled into self-standing or hybrid MBSs [6,7] by means of inter-module connections (IMCs). A particularly challenging scenario is met in tall self-standing steel MBSs, where connections between modules are part of the building's lateral load resisting systems (LLRS) and are subjected to more complex loading scenarios due to height-induced amplification of lateral load effects [8–10].

Hence, IMCs play a crucial role in the structural behaviour of MBSs by ensuring the vertical and horizontal load-transfer paths between modules, while also controlling the buildability of MBSs by embracing principles of design-for-assembly/-disassembly (DfA/DfD). Given that existing IMCs display limited disassembly opportunities and lack damage control features [11], there is reasonable scope for developing a new generation of hybrid, demountable IMCs that contribute effectively to the global damage distribution mechanism to improve the reuse chances of structural modules after exposure to demanding lateral loads such as strong winds or earthquakes.

In this regard the authors introduce a novel, hybrid IMC comprising bespoke corner fittings, a resilient high-damping rubber core and a pseudoelastic smart alloy bolt. The present study focuses on the development of a high-fidelity proof-of-concept finite element analysis (FEA) model used to identify the desired working mechanism and to characterise the mechanical behaviour of the proposed IMC subjected to tension and combined compression and shear loading. An extensive study done by the authors [12] provides further details regarding the ductility, energy dissipation and damping of the proposed connection, as well as a parametric FEA focused on the variation of bolt preload, endplate thickness, axial load magnitude and the vertical layout of the HDR core.

2. The hybrid inter-module connection (hybrid IMC)

The connection configuration illustrated in figure 1 consists of a high-damping rubber (HDR) core secured between the corner fittings of volumetric modules by means of a preloaded pseudoelastic shape-memory alloy (SMA) bolt.

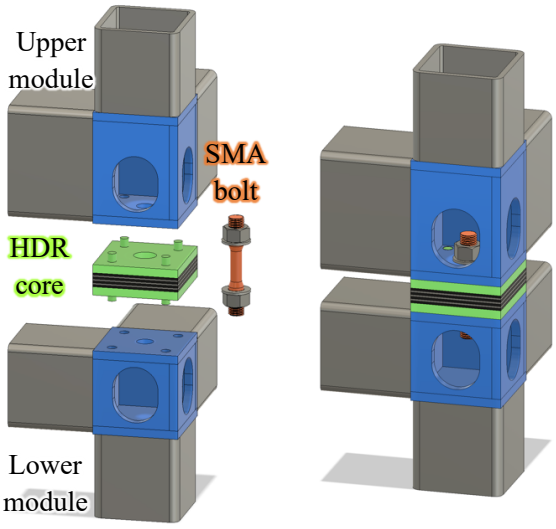

a) exploded view b) assembled joint

Figure 1. Configuration of the novel hybrid inter-module connection for a corner joint.

The system has been designed to fulfil the essential function of vertical and horizontal connectivity between modules, while also acting as a self-centring, energy dissipating component under uplift and combined compression and shear loading. The desired working mechanism of the novel IMC relies on a hybrid mechanical behaviour that fosters the unique material properties of its constituent components.

The HDR core consists of a laminated elastomeric bearing (LEB) designed to withstand the compressive stresses between the corners of modules by controlling the level of vertical displacement. Due to the innate high shear strength of engineering rubber, the bearing accommodates large inter-storey shear forces without failing, while the reduced shear stiffness alleviates the stress concentrations in the vicinity of the joint. The lateral displacement in the joint is limited above certain sway thresholds by the stiffening exhibited at high shear strains (S-shaped stress-strain curve), while the addition of carbon black fillers in the rubber mix (filled rubber) supplies the enhanced hysteresis (i.e., energy dissipation and damping) that characterises high-damping rubber (HDR) [13].

The shape-memory alloy (SMA) bolt complements the shear strength of the IMC by resisting the inter-storey drifts through a combined bending and shear action, yet the main advantage lies in the pseudoelasticity effect of SMAs which allows the bolt to develop large elastic strains during loading that are largely recoverable upon unloading. SMAs are a class of smart materials with physical properties similar to structural steel, capable of ‘memorising’ their shape due to the reversible transitions between its two main phases (i.e., martensite and austenite) caused by a shear lattice distortion mechanism [14]. SMA components in austenitic phase manifest a superelastic (or pseudoelastic) effect, characterised by a flag-shaped stress-strain curve with high load-unload stiffnesses and reduced permanent strains [15].

This effect equates to improved IMC resilience and demountability even after damage-inducing loading scenarios, as opposed to conventional high-strength steel bolts which either fail or become jammed due to permanent deformations. In addition, energy dissipation and damping are also supplied through hysteresis during the cyclic transition between austenite-martensite phases of the smart alloy.

The plug-in lugs on the outer plates of the bearing act as last-resort stoppers during late loading stages in the event of bolt fracture, ensuring a limited level of joint connectivity until the commencement of retrofitting works.

3. Methodology

3.1. Framework

The proof-of-concept connection tests have been carried out using validated, continuum finite element analysis (FEA) to determine the mechanical behaviour of the proposed IMC with respect to the main deformation modes expected to occur in the joints of tall steel MBSs under the combined effect of vertical and horizontal loading.

To calibrate the advanced material models required for capturing the viscoplastic behaviour of high-damping rubber (HDR) and the pseudoelastic (superelastic) behaviour of austenitic shape-memory alloys (SMAs), both materials were characterised through stress-strain and load-displacement curves extracted from specific experimental testing detailed below.

The ultra-high damping rubber compound from Tun Abdul Razak Research Centre (TARRC - http://tarrc.co.uk/) is adopted for the elastomeric layers of the LEB. Standard double-bonded shear tests have been carried out at TARRC on cylindrical test pieces made of two rubber layers hot-bonded to metal plates. The material model characterisation tests have been done at ambient temperature and the test pieces have been subjected to triangular waveforms up to +/-200% shear strain for 6 cycles at 10% strain rate (0.1/s) with a 2-minute wait before being subjected to triangular waveforms up to +/-200% shear strain for 1 cycle over an amplitude range of 25% shear strain with stress relaxation segments of 2 minutes inserted between each step change. The 6 consecutive cycles of +/- 200% shear strain have been done to account for the cumulative damage (also known as Mullins damage), such that the calibration was done on an already stabilised stress-strain behaviour of the HDR. The load-relax-load incremental steps are necessary for the calibration of the hysteresis parameters of the Bergström-Boyce model, which requires test data for at least two different strain rates to accurately predict the desired mechanical behaviour.

The SMA adopted is a Nickel-rich Nickel-Titanium alloy (Ni51-Ti49 % at.) supplied by the company 2SMArtEST Srl (https://2smartest.com/). The test samples have been heat treated at 500 °C for 30 min to adjust the final transformation temperatures (austenite finish temperature) and give proper superelastic behaviour at a practical range of temperatures for real-life applications.

Isothermal mechanical tests for material characterisation consisting of pseudo-static cyclic tensile tests with a monotonic strain controlled loading ($\dot{\varepsilon} = 3 \cdot 10^{-4}\ s^{-1}$) up to a given strain, ε_{tot}, followed by complete load-controlled unloading ($\dot{\sigma} = 12\ MPa \cdot s^{-1}$) have been performed at University of Calabria on standard dog-bone samples in fully austenitic conditions (T = 20 °C). The tests have been carried out using a universal testing machine (Instron E10000, USA) and strains have been measured by an extensometer (accuracy class 0.5 ISO) with a gauge length of 10 mm.

3.2. Finite Element Models

The computational analyses in the present study have been conducted using the standard (implicit) solver of commercial FEA package Abaqus® [16] including geometric, material and boundary nonlinearities.

The steel connection components are based on typical sizes of modular framing members reported in the literature [17], while the design of the HDR core and SMA bolt has been based on provisions for elastomeric bearings as per EN 1337-3 [18] and recommendations from experimental observations on threaded SMA bars [14] respectively. The detailed drawings of all connection parts are illustrated in figure 2.

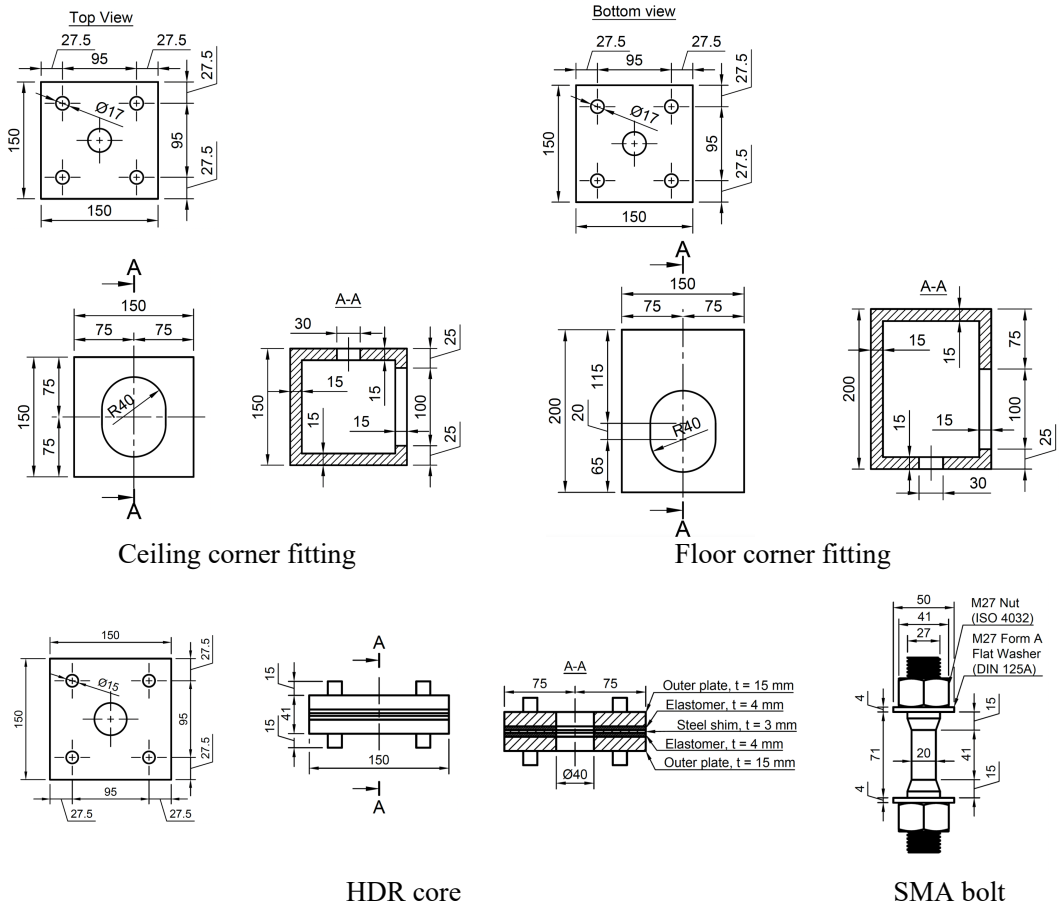

Figure 2. Detailed drawings of connection components.

For contact interactions, normal behaviour is defined using the nonlinear, penalty-enforced, "Hard" pressure-overclosure relationship, while for tangential direction, the default penalty friction formulation based on the basic Coulomb friction model is adopted. The friction coefficient is taken as $\mu = 0.3$, assuming steel-to-steel interfaces that have been cleaned by wire-brushing or flame cleaning, with loose rust removed as per EN-1090-2 [19].

General static steps are defined for each loading stage. The initial bolt preload is applied during the first step in both tension and shear FEA. To provide initial stiffness without affecting the ductility and re-centring capability, the bolt pre-stress is limited to 50% of the forward transformation start stress, σ_{Ms}, resulting in a preload force $F_{p.C}$ = 80 kN. For the tension FEA setup, a displacement-controlled vertical load is applied during the second step, while for the shear FEA a compressive axial load is applied in the second step to simulate the effect of permanent gravitational loading, followed by a displacement-controlled horizontal shear loading during the third step. The compressive axial load has been taken as N_{Ed} = 97.5 kN, equal to 5% of the compressive yield capacity ($N_{c.Rd}$) of the column's cross-section. Loading and boundary conditions are applied using reference points coupled to cross-sections with distributed continuum coupling constraints, while the bolt load is defined through an orthogonal surface passing through the middle of the bolt's shank. The cyclic loading histories in figure 3 are based on the EN 15129 [20] load protocol using the maximum displacement as the design displacement, corresponding to the displacement at which the stress in the bolt's shank reaches the finish transformation stress, σ_{Mf}. The maximum displacement, Δ_{max}, has been determined through an initial monotonic load sequence up to Δ_{max} for each load case considered.

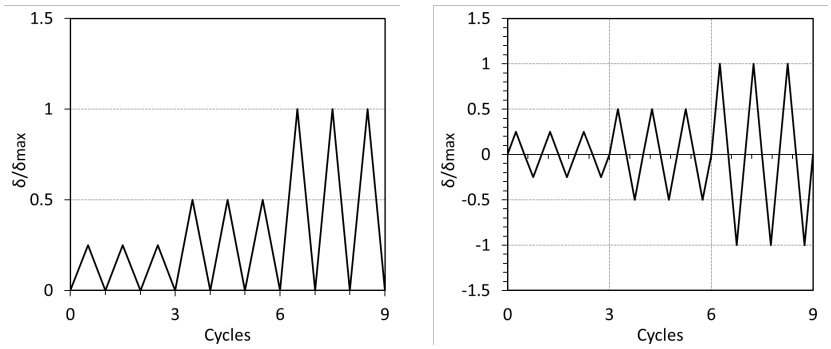

Figure 3. Cyclic loading histories

The steel and SMA parts have been meshed with first-order 8-node linear brick (3D solid) elements (C3D8R) with reduced integration, while the steel plates in the HDR core have been meshed with the equivalent hybrid elements (C3D8RH). The rubber layers have been meshed with fully integrated first-order 8-node hybrid linear brick elements (C3D8H). The adequate mesh refinement has been explored in terms of accuracy of results versus analysis efficiency through a rigorous sensitivity analysis. An overview of the final FEA model setup and mesh details is illustrated in figure 4**.**

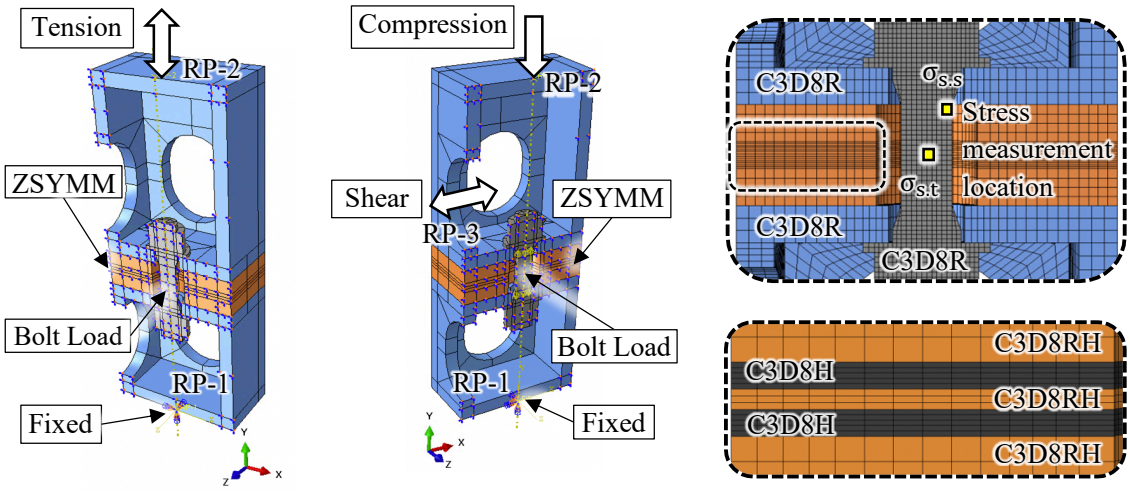

(a) tension load case

(b) combined compression and shear load case

(c) mesh details

Figure 4. FEA model setup.

3.3. Material models

The FEA model includes three different materials, namely structural steel, high-damping rubber and pseudoelastic SMA, each presenting specific characteristics in their constitutive models.

Structural steel has been modelled using the standardised bi-linear plus nonlinear isotropic hardening model proposed by Yun and Gardner [21] due to its practicality. The model accurately depicts the stress-strain response of steel based just on the three basic material parameters readily available in design codes, namely the modulus of elasticity E, the yield strength f_y, and the ultimate strength f_u. Material parameters used to characterise the elasto-plastic behaviour of steel grade S355 (table 1) have been taken from Eurocode 3 [22] based on nominal material properties and nominal element thickness $t \leq 40$ mm.

Table 1. Nominal material properties for steel grade S355.

Steel grade	ρ[a] (kg/m^3)	E (N/mm^2)	ν[b] (-)	f_y (N/mm^2)	f_u (N/mm^2)	ε_u[c] (%)
S355	7,850	210,000	0.3	355	490	16.53

[a] Density of steel
[b] Poisson's ratio
[c] Ultimate strain

To capture the non-linear viscoelastic (non-LVE) response of high-damping rubber, the Bergström-Boyce (BB) model based on Yeoh hyperelasticity has been used. The calibration of the material model has been performed using the commercial material parameter extraction tool MCalibration [23], with the final material parameters summarised in table 2.

Table 2. Material properties for high-damping rubber.

Model	Hyperelasticity coefficients						Non-linear viscoelasticity (Bergström-Boyce)				NMAD[g] Fitness
							SF[c]	A[d]	m[e]	C[f]	
Yeoh	C_{10}[a] 0.139	C_{20}[a] -0.014	C_{30}[a] 0.003	D_1[b] 0	D_2[b] 0	D_3[b] 0	24.7	141.4	10.85	-0.99	8.2 %

[a] Stiffness coefficients
[b] Compressibility coefficients taken as 0 to approximate fully incompressible behaviour of elastomers
[c] Stress scaling factor
[d] Creep parameter
[e] Effective stress exponent
[f] Creep strain exponent
[g] Normalized Mean Absolute Difference/Error

The typical flag-shaped constitutive behaviour of pseudoelastic SMA under isothermal conditions has been modelled through the combination of elasticity (for the austenite phase) and superelasticity (for the martensite phase) using a built-in material model based Auricchio and Taylor's work [24,25]. This model has been widely adopted in the literature and has accurately reflected the mechanical behaviour of Ni-Ti based SMA bars [26–28]. The material parameters used to model the superelastic SMA have been extracted from the first load-unload cycle of the experimental stress-strain curve and are presented in table 3.

Table 3. Material properties for pseudoelastic SMA.

E_A[a] (MPa)	E_M[b] (MPa)	ν_A[c] (-)	ν_M[d] (-)	σ_{M_s}[e] (MPa)	σ_{M_f}[f] (MPa)	σ_{A_s}[g] (MPa)	σ_{A_f}[h] (MPa)	ε_L[i] (%)
87500	38438	0.33	0.33	525	615	180	90	3.64

[a] Young's modulus of austenite.
[b] Young's modulus of martensite.
[c] Poisson's ratio of austenite.
[d] Poisson's ratio of martensite.
[e] Forward (load) transformation start stress.
[f] Forward (load) transformation finish stress.
[g] Reverse (unload) transformation start stress.
[i] Reverse (unload) transformation finish stress.
[h] Total transformation strain.

3.4. FEA Validation

The FEA modelling techniques have been validated by simulating experimental tests on three separate IMCs studied by Chen et al [29] in figure 5 (a), Lacey et al. [30] in figure 5 (b), and Chen et al [31] in figure 5 (c) and the laminated elastomeric bearing (LEB) studied by Rahnavard and Thomas [32] in figure 5 (d). In addition, the validation of the calibrated material models presented in the previous section is also completed by simulating the experimental characterisation tests for rubber in figure 5 (e) and SMA in figure 5 (f). Overall, the validation results presented herein demonstrate the high accuracy of the present FEA modelling techniques, further supporting their use for predicting the mechanical behaviour of the proposed hybrid IMC.

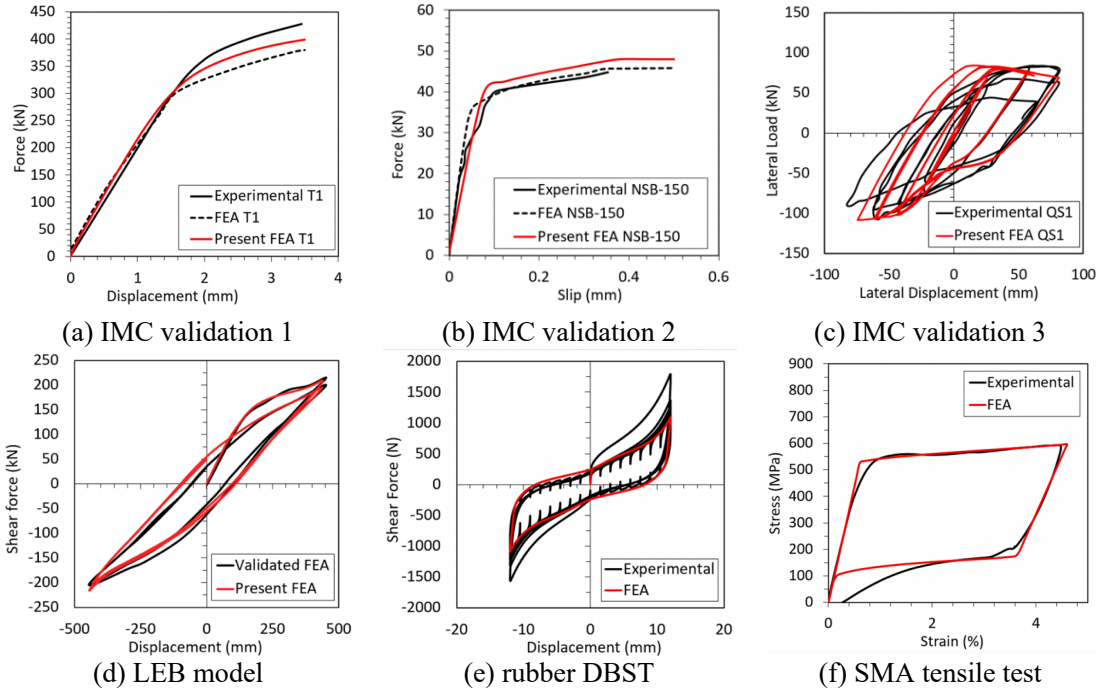

(a) IMC validation 1 (b) IMC validation 2 (c) IMC validation 3

(d) LEB model (e) rubber DBST (f) SMA tensile test

Figure 5. FEA validation studies.

4. FEA Results

4.1. Tension behaviour

The main deformation modes and stress states of the hybrid IMC under cyclic tension loading are illustrated in figure 6.

The stress contour in figure 6 (a) shows the Mises stress in the bolt's shank, corresponding to the start of "yield"-like point, just as the stress overcomes the forward transformation start stress, $\sigma_{Ms} = 525$ MPa. As the applied tensile displacement increases (figure 6 (b)), the inelastic stress concentrates uniformly in the bolt's shank, up to the ultimate/maximum point corresponding to the stress contours in the SMA bolt's shank reaching the forward transformation finish stress $\sigma_{Mf} = 615$ MPa. Figure 6 (c) shows the Mises plots limited by the yield strength of S355 steel, $f_y = 355$ MPa, indicating stress concentrations near bolt holes in the steel endplates of corner fittings, while the actual values barely exceed the yield limit. These results indicate that the hybrid IMC achieves the desired working mechanism in tension, as the tensile axial loading is mainly resisted by the SMA bolt, while the contribution of the endplates bending remains negligible.

This observation is further supported by the equivalent plastic strain (PEEQ) contours in figure 6 (d), in which the non-zero values represent very limited regions where the steel has sustained plastic

deformation. The figures reveal that the plastic regions at the end of the third cycle of maximum tensile loading are localised towards the inner sides of the IMC, at interface between endplates and the outer plates of the HDR core, caused by the sudden section change as part of the endplates near bolt hole rims cantilever over the larger hole in the HDR core.

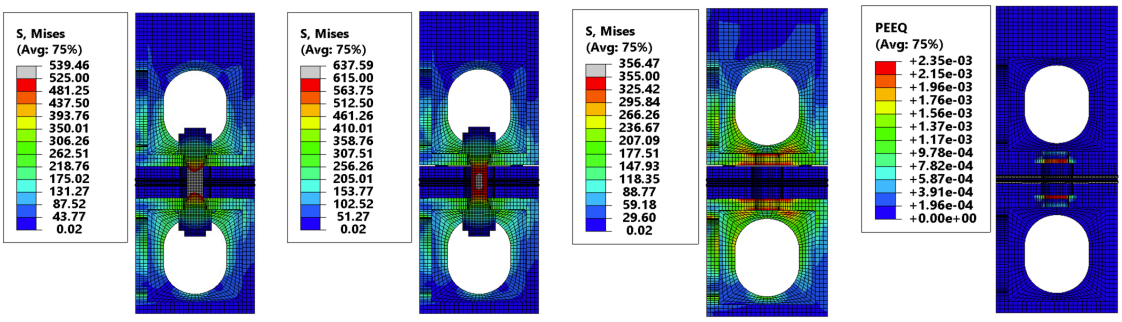

(a) $+\delta_{t.y}$ = 1.11 mm (b) $+\delta_{t.max}$ = 2.48 mm (c) $+\delta_{t.max}$ = 2.48 mm (d) 3rd $+\delta/\delta_{max}$ = 1

Figure 6. Mises stress plots and PEEQ contours under cyclic tension loading.

The hysteresis loop corresponding to the stress states and deformation modes under tension loading is illustrated in figure 7 (a), while the main mechanical parameters are extracted in table 4. The loop's flag-shape is a good qualitative indication of the connection's good energy dissipation capacity due to the transformation-induced pseudoelastic deformations in the SMA bolt, while a self-centring effect with limited residual displacements is also present. The blue dashed curve represents the initial monotonic loading performed to determine the maximum displacement used for tailoring the cyclic loading protocols for each of the tested specimens. The generic force-displacement curve is illustrated in figure 7 (b) and comprises four characteristic stages governed by key changes in the stress-strain response of the SMA bolt. Since stress state beyond the martensite transformation point equates to the development of permanent inelastic strains in the SMA, it is desired to keep the mechanical response of the connection within the first three stages to maintain the re-centring effect under tension loading and the post-load demountability of the hybrid IMC. The overall shape and stages that characterise the force-displacement behaviour of the hybrid IMC in tension are in good agreement with previous findings reported in the literature [33–35].

Table 4. Mechanical parameters extracted from tension FEA.

$F_{t.0}$[a] (kN)	$\delta_{t.0}$[b] (mm)	k_I[c] (kN/mm)	$F_{t.y}$[d] (kN)	$\delta_{t.y}$[e] (mm)	k_{II}[f] (kN/mm)	$F_{t.max}$[g] (kN)	$\delta_{t.max}$[h] (mm)	k_{III}[i] (kN/mm)
44.27	0.08	610.44	168.05	1.11	119.80	181.07	2.48	9.50

[a] Initial tension strength.
[b] Initial displacement.
[c] First stage stiffness.
[d] Yield-like tension strength.
[e] Yield-like displacement.
[f] Second stage stiffness.
[g] Maximum tension strength.
[i] Maximum displacement.
[h] Third stage stiffness.

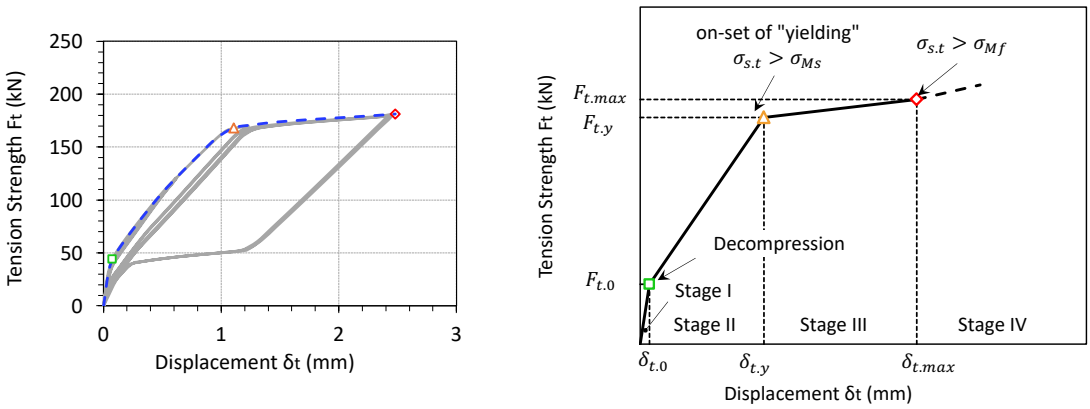

(a) Hysteresis loop (b) Idealised F-d curve

Figure 7. Load-displacement response under cyclic tension loading.

4.2. Combined compression shear behaviour

The main deformation modes and stress states occurring in the IMC during combined compression-shear loading are illustrated in figure 8. The contours plotted in figure 8 (a) show the Mises stress in the hybrid IMC when the shear displacement reaches the onset of slipping, $\delta_{s.os}$. At this point, the initial gap of 1.5 mm due to the 3 mm bolt hole clearance provided in the corner fittings is still unchanged, while the two diagonally opposite shank regions which exceeded the forward transformation start stress, $\sigma_{Ms} = 525$ MPa, are a sign of the bolt's main deformation mode defined as combined bending and shear. As the shear displacement increases and the bolt begins to slide, closing the clearance gap (figure 8 (b)), the stress in the bolt shank decreases below σ_{Ms}. At this stage the end of slipping displacement, $\delta_{s.es}$, is reached as the bolt shank has come into full contact with the bolt hole walls in the corner fitting. Further loading beyond this point resumes the development of stress in the tension side of the shank up until the forward transformation finish stress, σ_{Mf}, is eventually exceeded at the peak shear displacement, $\delta_{s.max}$ (figure 8 (c)).

As explained in the case of pure tension loading, the hybrid IMC is intended to work only within the pseudoelastic limits of the SMA bolt, hence σ_{Mf} governs the ultimate limit of the mechanical behaviour during combined compression-shear loading as well. Overall, the stress evolution indicates that the hybrid IMC achieves the desired working mechanism in combined compression-shear, as the stress mainly develops in the SMA pin by virtue of the HDR core's flexibility in shear which prevents the direct bearing of corner fittings, keeping the stress levels in the module members negligible.

The equivalent plastic strain (PEEQ) contours illustrated in figure 8 (d) reveal that the plastic regions at the end of the third cycle of peak shear displacement are localised around the rims of the bolt holes in the corner fitting endplates and are caused by the high contact pressure that acts repetitively upon these surfaces as the SMA pin slides from side to side during cyclic shear loading.

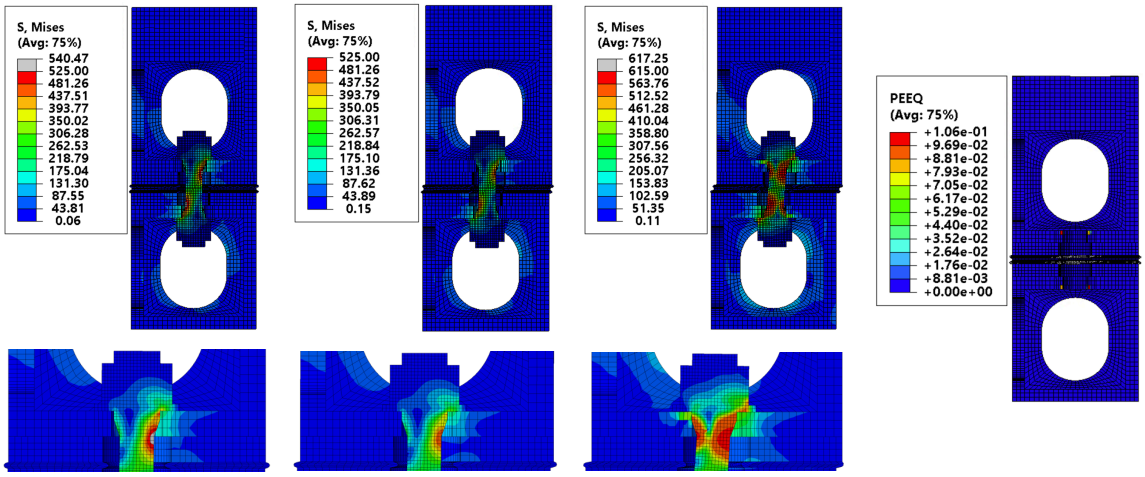

(a) $+\delta_{s.os}$ = 1.00 mm (b) $+\delta_{s.es}$ = 3.75 mm (c) $+\delta_{s.max}$ = 7.25 mm (d) 3rd $+\delta/\delta_{max}$ = 1

Figure 8. Mises stress plots and PEEQ contours under combined compression and cyclic shear.

To facilitate the qualitative and quantitative assessment of the cyclic shear response of the hybrid IMC, the hysteresis loop is plotted in figure 9 (a), while corresponding mechanical parameters are extracted in table 5. The generic force-displacement curve is illustrated in figure 9 (b) and comprises four characteristic stages governed by the IMC slip behaviour and key changes in the stress-strain response of the SMA bolt. As defined for the tension behaviour, Stage IV reaches beyond the upper limit of the pseudoelastic response in the SMA pin and is considered outside of the safe working mechanism intended for the proposed design.

The curves in figure 9 (c) show the force contribution of the SMA bolt and HDR core when loaded up to a shear displacement of + 8 mm, while the corresponding maximum shear strengths of each component, F_{SMA} = 45.11 kN, F_{HDR} = 12.43 kN, are in good agreement with the total F_{IMC} = 57.02 kN (error < 1%). From the graph, it is confirmed that in the current design the SMA pin provides the major contribution to the total shear response of the hybrid IMC (i.e., 79.1%) while the HDR core plays a secondary role.

Table 5. Mechanical parameters extracted from combined compression and shear FEA.

$F_{s.os}$[a] (kN)	$\delta_{s.os}$[b] (mm)	k_I[c] (kN/mm)	$F_{s.es}$[d] (kN)	$\delta_{s.es}$[e] (mm)	k_{II}[f] (kN/mm)	$F_{s.max}$[g] (kN)	$\delta_{s.max}$[h] (mm)	k_{III}[i] (kN/mm)
24.25	1.00	24.25	26.27	3.75	0.73	54.43	7.25	8.05

[a] Onset of slipping strength.
[b] Onset of slipping displacement.
[c] First stage stiffness.
[d] End of slipping strength.
[e] End of slipping displacement.
[f] Second stage stiffness.
[g] Maximum shear strength.
[i] Maximum displacement.
[h] Third stage stiffness.

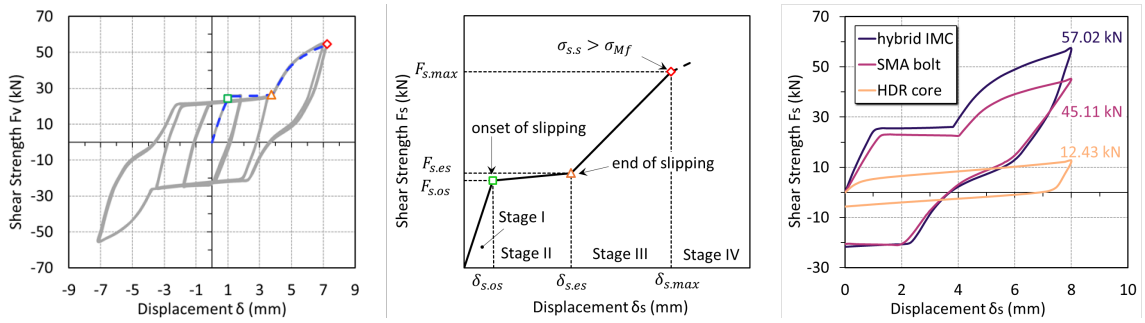

(a) Hysteresis loop (b) Idealised F-d curve (c) Individual contribution

Figure 9. Load-displacement response under combined compression and shear loading.

5. Concluding remarks

In the present study a novel hybrid IMC has been proposed and its tension and combined compression and shear behaviours are studied and quantified by means of validated high-fidelity FEA. The key points are summarised as follows.

The hybrid IMC's tension behaviour is governed by the stress-strain response of the SMA pin, demonstrating a robust cyclic performance with effective re-centring effects and is divided into four separate load stages corresponding to transformation-induced stress changes suffered by the bolt.

The combined compression-shear behaviour of the proposed IMC relies on the effectiveness of the resilient HDR core to undergo large shear straining without failing, while the main resistance is provided by a combined shear-bending deformation state in the SMA pin's shank.

The total shear response has been successfully decoupled, revealing the major contribution of the SMA bolt regarding recoverable deformation, while the HDR core plays a supporting role.

Due to the effective contribution of each component to the combined hybrid response, the connection succeeds in preventing the formation of significant plastic damage in the MBS's corner fittings to facilitate reusability of modules, while the resilience and demountability of the IMC are ensured provided that the SMA pin is designed to work within the pseudoelastic domain.

Acknowledgements

The authors would like to thank Mr Carmine Maletta, Professor of Machine Design at University of Calabria and CEO of 2SMArteST, and Mr Fabrizio Niccoli, Researcher at University of Calabria and CTO of 2SMArtEST for their very valuable and continuous technical support. Their experience and expertise have been instrumental to the material characterisation and fabrication of the pseudoelastic shape-memory alloy bolts. The authors would also like to thank Mr Hamid Ahmadi, Head of Division at TARRC, for his technical support with regards to the material characterisation and fabrication of high-damping rubber cores.

6. References

[1] Gorgolewski M T, Grubb P J and Lawson R M 2001 *Modular Construction using Light Steel Framing: Design of Residential Buildings* (Ascot: SCI)

[2] Ahn Y H and Kim K-T 2015 Sustainability in modular design and construction: a case study of 'The Stack.' *Int. J. Sustain. Build. Technol. Urban Dev.* **5** 250–9

[3] Jabar I I, Ismail F, Mustafa A A 2013 Issues in Managing Construction Phase of IBS Projects *Procedia Soc. Behav. Sci.* **101** 81–9

[4] Nahmens I and Ikuma L H 2012 Effects of Lean Construction on Sustainability of Modular Homebuilding *J. Archit. Eng.* **18** 155–63

[5] Kamali M and Hewage K 2016 Life cycle performance of modular buildings: A critical review *Renewable Sustainable Energy Rev.* **62** 1171–83

[6] Hough M J and Lawson R M 2019 Design and construction of high-rise modular buildings based on recent projects. *Proc. Inst. Civ. Eng.: Civ. Eng.* **172** 37–44

[7] Lawson R M and Richards J 2010 Modular design for high-rise buildings. *Proc. Inst. Civ. Eng.: Struct. Build.* **163** 151–64
[8] Lacey A W, Chen W, Hao H and Bi K 2013 Effect of inter-module connection stiffness on structural response of a modular steel building subjected to wind and earthquake load *Eng. Struct.* **213** 110628
[9] Wang Z and Tsavdaridis K D 2022 Optimality criteria-based minimum-weight design method for modular building systems subjected to generalised stiffness constraints: A comparative study *Eng. Struct.* **251** 113472
[10] Farajian M, Sharafi P, Eslamnia H, Kildashti K and Bai Y 2022 Classification of inter-modular connections for stiffness and strength in sway corner-supported steel modular frames *J. Constr. Steel Res.* **197** 107458
[11] Corfar D-A and Tsavdaridis K D 2022 A comprehensive review and classification of inter-module connections for hot-rolled steel modular building systems *J. Build. Eng.* **50** 104006
[12] Corfar D-A and Tsavdaridis K D 2023 A Hybrid Inter-Module Connection for Steel Modular Building Systems with SMA and High-Damping Rubber Components *Eng. Struct.* submitted
[13] Lindley P B 2015 *Engineering Design with Rubber* (Hertford: TARRC)
[14] Fang C and Wang W 2020 *Shape Memory Alloys for Seismic Resilience* (Singapore: Springer)
[15] Abavisani I, Rezaifar O and Kheyroddin A 2021 Multifunctional properties of shape memory materials in civil engineering applications: A state-of-the-art review. *J. Build. Eng.* **44** 102657
[16] Dassault Systèmes SIMULIA Corp 2020 Abaqus CAE
[17] Lawson R M, Ogden R G and Goodier C 2014 *Design in Modular Construction* (Oxon: CRC Press)
[18] BSI 2006 *Structural bearings — Part 3: Elastomeric bearings* (London: BSI)
[19] BSI 2018 *Execution of steel structures and aluminium structures - Part 2: Technical requirements for steel structures* (London: BSI)
[20] BSI 2018 *Anti-seismic devices* (London: BSI)
[21] Yun X and Gardner L 2017 Stress-strain curves for hot-rolled steels *J. Constr. Steel Res.* **133** 36–46
[22] BSI 2015 *Eurocode 3: Design of steel structures - Part 1-1: General rules and rules for buildings* (London: BSI)
[23] PolymerFEM 2023 MCalibration
[24] Auricchio F and Taylor R L 1997 Shape-memory alloys: modelling and numerical simulations of the finite-strain superelastic behavior *Comput. Methods Appl. Mech. Eng.* **143** 175–94
[25] Auricchio F, Taylor R L and Lubliner J 1997 Shape-memory alloys: macromodelling and numerical simulations of the superelastic behavior *Computer Methods in Applied Mechanics and Engineering* **146** 281–312
[26] Askariani S S, Garivani S, Hajirasouliha I and Soleimanian N 2022 Innovative self-centering systems using shape memory alloy bolts and energy dissipating devices *J. Constr. Steel. Res.* **190** 107127
[27] Qiu C, Liu J and Du X 2022 Cyclic behavior of SMA slip friction damper *Eng. Struct.* **250** 113407
[28] Chen J, Wang W and Fang C 2022 Manufacturing, testing and simulation of novel SMA-based variable friction dampers with enhanced deformability *J. Build. Eng.* **45** 103513
[29] Chen Z, Wang J, Liu J and Cong Z 2020 Tensile and shear performance of rotary inter-module connection for modular steel buildings *J. Constr. Steel Res.* **175** 106367
[30] Lacey A W, Chen W, Hao H, Bi K and Tallowin F J 2019 Shear behaviour of post-tensioned inter-module connection for modular steel buildings *J. Constr. Steel Res.* **162** 105707
[31] Chen Z, Liu J, Yu Y, Zhou C and Yan R 2017 Experimental study of an innovative modular steel building connection *J. Constr. Steel Res.* **139** 69–82
[32] Rahnavard R and Thomas R J 2019 Numerical evaluation of steel-rubber isolator with single and multiple rubber cores *Eng. Struct.* **198** 109532

[33] Fang C, Wang W, He C and Chen Y 2017 Self-centring behaviour of steel and steel-concrete composite connections equipped with NiTi SMA bolts *Eng. Struct.* **150** 390–408
[34] Wang B, Nishiyama M, Zhu S, Tani M and Jiang H 2020 Development of novel self-centering steel coupling beams without beam elongation for earthquake resilience *Eng. Struct.* **232** 111827
[35] Wang B, Jiang H and Wang J 2019 Numerical simulation and behavior insights of steel columns with SMA bolts towards earthquake resilience *J. Constr. Steel Res.* **161** 285–95